The Astrophysical Journal Letters, 901:L13 (6pp), 2020 September 20 https://doi.org/10.3847/2041-8213/abb535

Pair Separation in Parallel Electric Field in Magnetar Magnetosphere and Narrow Spectra of Fast Radio Bursts

Yuan-Pei Yang[1], Jin-Ping Zhu[2,3], Bing Zhang[4], and Xue-Feng Wu[5]
[1] South-Western Institute for Astronomy Research, Yunnan University, Kunming 650500, Yunnan, People's Republic of China; ypyang@ynu.edu.cn
[2] Kavli Institute for Astronomy and Astrophysics, Peking University, Beijing 100871, People's Republic of China
[3] Department of Astronomy, School of Physics, Peking University, Beijing 100871, People's Republic of China
[4] Department of Physics and Astronomy, University of Nevada, Las Vegas, NV 89154, USA; zhang@physics.unlv.edu
[5] Purple Mountain Observatory, Chinese Academy of Sciences, Nanjing 210023, People's Republic of China
Received 2020 June 5; revised 2020 July 22; accepted 2020 September 3; published 2020 September 22

Abstract

When the magnetosphere of a magnetar is perturbed by crustal deformation, an electric field $E_{\parallel}$ parallel to the magnetic field line would appear via Alfvén waves in the charge starvation region. The electron–positron pair bunches will be generated via two-stream instability in the magnetosphere, and these pairs will undergo charge separation in the $E_{\parallel}$ and in the meantime emit coherent curvature radiation. Following the approach of Yang & Zhang, we find that the superposed curvature radiation becomes narrower due to charge separation, with the width of spectrum depending on the separation between the electron and positron clumps. This mechanism can interpret the narrow spectra of fast radio bursts (FRBs), in particular, the spectrum of Galactic FRB 200428 recently detected in association with a hard X-ray burst from the Galactic magnetar SGR J1935+2154.

Unified Astronomy Thesaurus concepts: Radio transient sources (2008); Galactic radio sources (571); Radio bursts (1339); Magnetars (992)

1. Introduction

Fast radio bursts (FRBs) are mysterious radio transients with millisecond durations and extremely high brightness temperatures from cosmological distances (Lorimer et al. 2007; Thornton et al. 2013; Chatterjee et al. 2017; Bannister et al. 2019; Prochaska et al. 2019; Ravi et al. 2019; Marcote et al. 2020). Recently, an FRB-like event (FRB 200428) with two peaks separated by 30 ms (Bochenek et al. 2020; The CHIME/FRB Collaboration et al. 2020) was detected from the Galactic magnetar, SGR J1935+2154, during its active phase in association with a hard X-ray burst (Li et al. 2020; Mereghetti et al. 2020; Ridnaia et al. 2020; Tavani et al. 2020). The Canadian Hydrogen Intensity Mapping Experiment (CHIME) detected FRB 200428 at (400–800) MHz with a dispersion measure DM $= 333\,\mathrm{pc\,cm^{-3}}$ and a fluence reaching a few hundreds of kJy ms (The CHIME/FRB Collaboration et al. 2020). Meanwhile, the Survey for Transient Astronomical Radio Emission 2 (STARE2) reported the simultaneous detection of one of the two peaks (likely the second peak) of FRB 200428 with an extremely large fluence reaching $\sim$1.5 MJy ms at 1.4 GHz, which is about 40 times less energetic compared with the weakest extragalactic FRBs observed so far (Bochenek et al. 2020). The associated hard X-ray burst was detected by Insight-HXMT (Li et al. 2020), INTEGRAL (Mereghetti et al. 2020), Konus-Wind (Ridnaia et al. 2020), and AGILE (Tavani et al. 2020). In particular, there are two hard X-ray peaks whose arrival times are consistent with the two FRB peaks after de-dispersion (Li et al. 2020; Ridnaia et al. 2020).

Although FRB 200428 was found to be associated with a hard X-ray burst, deep searches by the Five-hundred-meter Aperture Spherical Telescope for FRBs revealed no single detection, even during the epochs when 29 soft-γ-ray bursts were detected by Fermi GBM (Lin et al. 2020). This suggests that the FRB–soft gamma-ray repeater (SGR) association is very rare. Among other possibilities, the low probability of association could be due to the narrow spectra of FRBs (Lin et al. 2020). Such narrow spectra have been hinted by the extreme variation of spectral indices among different bursts of FRB 121102 (Spitler et al. 2016) as well as the relative fluence of the two peaks of FRB 200428 as observed by CHIME and STARE2.

The association between FRB 200428 and the two hard spikes of the X-ray burst from SGR J1935+2154 suggests that they very likely share the same origin. The high-energy emission from a magnetar is widely interpreted as due to magnetospheric activity (Thompson & Beloborodov 2005; Beloborodov & Thompson 2007). When a magnetar magnetosphere is triggered by crustal deformations, an electric field $E_{\parallel}$ parallel to the magnetic field line would appear via Alfvén waves in the charge starvation region (Kumar & Bošnjak 2020; Lu et al. 2020). The electron–positron pair bunches will be generated via two-stream instability in the magnetosphere, and these pairs will undergo charge separation in $E_{\parallel}$ and emit coherent curvature radiation. In this work, we calculate the coherent curvature radiation spectrum of spatially separated pairs, and apply it to the observed spectra of FRB 200428. The Letter is organized as follows. We first discuss the FRB generation mechanism within the magnetosphere of a magnetar in Section 2. We then calculate the coherent curvature radiation spectra of the separated pair clumps in Section 3. The results are summarized in Section 4. The convention $Q_x \equiv Q/10^x$ is adopted in cgs units.

2. FRBs from Magnetosphere Activities

Various FRB models can be divided into "far-way" models and "close-in" models based on the distance of the emission region from the neutron star (Lu et al. 2020). The former suggests that the energy is dissipated via an outflow interacting with the ambient medium, and radio emission is produced by certain synchrotron maser mechanisms (Lyubarsky 2014; Beloborodov 2017, 2020; Waxman 2017;

Metzger et al. 2019; Margalit et al. 2020; Yu et al. 2020; Wu et al. 2020). The latter suggests that the radio emission is from the magnetosphere of a neutron star (Pen & Connor 2015; Cordes & Wasserman 2016; Katz 2016; Kumar et al. 2017; Zhang 2017; Lu & Kumar 2018; Yang & Zhang 2018; Dai 2020; Kumar & Bošnjak 2020; Lu et al. 2020; Wang et al. 2020; Wang 2020). We believe that a magnetospheric origin of FRB emission is most likely, based on the following observational evidence or theoretical arguments. The issues of the synchrotron maser model to interpret FRB 200428 have been discussed by Lu et al. (2020) (see Margalit et al. 2020).

1. The two pulses of FRB 200428 (The CHIME/FRB Collaboration et al. 2020) were associated with two hard spikes of the hard X-ray burst from SGR J1935+2154 (Li et al. 2020; Ridnaia et al. 2020). The high-energy emission of SGRs has been widely believed to be caused by the magnetosphere activity of the magnetars (Thompson & Beloborodov 2005; Beloborodov & Thompson 2007). It is most natural to attribute the radio emission as also from the magnetosphere (Li et al. 2020).
2. Several magnetars have been identified as pulsed radio emitters (Camilo et al. 2006, 2007), e.g., XTE J1810-197 and 1E 1547.0-5408. The coherent radio emission of these magnetars is well consistent with being due to a magnetospheric origin (Wang et al. 2019a).
3. The observation of the frequency drift of FRB 121102 is $\dot{\nu} \sim (10\text{–}10^3)$ MHz ms^{-1} at $\nu \sim 1$ GHz (Hessels et al. 2019). This information may be used to estimate the size of the emission region

$$r \sim \frac{c\nu}{\dot{\nu}} \lesssim 10^9 \text{ cm}, \tag{1}$$

which is smaller than the light cylinder $R_{\rm LC} = cP/2\pi \simeq 5 \times 10^9$ cm P_0 of a neutron star. Indeed, such a drifting behavior can be well interpreted within the framework of magnetospheric coherent curvature radiation models (Wang et al. 2019b).

Coherent curvature radiation by bunches could be an attractive mechanism to generate FRBs from the magnetosphere of a magnetar (e.g., Kumar et al. 2017; Yang & Zhang 2018; Lu et al. 2020). For an FRB at $\nu \sim 1$ GHz, the electron (positron) Lorentz factor is required to be

$$\gamma = \left(\frac{4\pi\rho\nu}{3c}\right)^{1/3} \sim 520\rho_9^{1/3}, \tag{2}$$

where the curvature radius is about $\rho \sim 4r/3\theta$, and θ is the poloidal angle. The rapid cooling of the leptons in the coherent bunch demands that there should be an electric field ($E_\parallel$) along the magnetic field lines to continuously provide emission power (Kumar et al. 2017). In non-twisted pulsar magnetospheres, such an $E_\parallel$ may be generated by a deficit of charge density with respect to the Goldreich–Julian density—the so-called gaps (e.g., Ruderman & Sutherland 1975; Arons & Scharlemann 1979). Magnetar magnetospheres are widely believed to be current-carrying and twisted (e.g., Thompson et al. 2002; Beloborodov 2009). A high-density pair plasma is expected to fill the magnetosphere so that no global $E_\parallel$ is expected (Thompson et al. 2002; see Wadiasingh et al. 2020). Additional mechanisms are needed to generate $E_\parallel$. One possibility is that a strong $E_\parallel$ can be induced as Alfvén waves reach a critical radius where charge starvation occurs (Kumar & Bošnjak 2020; Lu et al. 2020). Particle acceleration occurs and an FRB can be generated. The balance between acceleration and radiation cooling requires

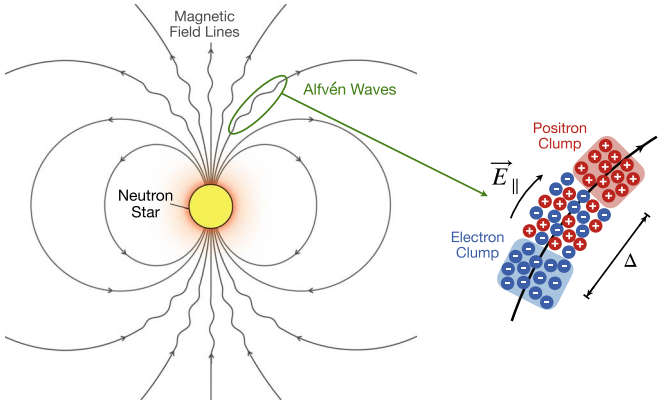

Figure 1. Illustration of the magnetospheric FRB model (see also Lu et al. 2020). The green ellipse denotes the region where $E_\parallel$ is developed and charges separate. The red points denote the leading positron clump, and the blue points denote the trailing electron clump. Δ is the separation between the clump pair. $E_\parallel$ is triggered by Alfvén waves reaching the charge starvation region (Kumar & Bošnjak 2020).

$$NeE_\parallel c \sim \eta N^2 \frac{2e^2 c\gamma^4}{3\rho^2}, \tag{3}$$

where N is the electron number in a coherent bunch, and $\eta \leqslant 1$ is a coherence factor we introduced. In previous estimations, $\eta = 1$ has been assumed so that the radiation power of curvature radiation is N^2 times than that of a single electron. This is strictly speaking the case when N electrons are regarded as a point source. Considering realistic bunches in three-dimensional scales, its radiation would be somewhat suppressed due to incoherence, leading to $\eta < 1$ (see detailed discussions in Yang & Zhang 2018).

For a pair plasma, the existence of the $E_\parallel$ makes electrons and positrons decouple and separate from each other, as shown in Figure 1. This would lead to two-stream instability that facilitates the formation of clumps of particles (see detailed discussions in Kumar et al. 2017; Kumar & Bošnjak 2020). In the meantime, a Coulomb field is generated due to pair separation. For an order of magnitude treatment, we approximate the positron and electron clumps as point sources with a separation of Δ, and assume that the pair clumps keep balance under electric field acceleration and radiation cooling. Without loss of generality, we assume an antiparallel rotator so that the Goldreich–Julian charge density is positive in the polar region. The Alfvén waves will induce an outward $E_\parallel$. Considering this $E_\parallel$ and the secondary Coulomb field due to charge separation, the balance condition of both clumps can be written as

$$E_\parallel - \frac{N_- e}{\Delta^2} \sim \eta N_+ \frac{2e\gamma^4}{3\rho^2}, \quad \text{for positron clump,} \tag{4}$$

$$\frac{N_+ e}{\Delta^2} - E_\parallel \sim \eta N_- \frac{2e\gamma^4}{3\rho^2}, \quad \text{for electron clump,} \tag{5}$$

where N_+ and N_- are the particle numbers in the positron and electron clumps, respectively. Eliminating $E_\parallel$ in the above

equations, one gets

$$\Delta \sim \left(\frac{3}{2\eta\mathcal{M}}\right)^{1/2}\frac{\rho}{\gamma^2} \sim 12\ \mathrm{cm}\ \mathcal{M}_4^{-1/2}\eta^{-1/2}\rho_9\gamma_3^{-2} \quad (6)$$

where $\mathcal{M} = (N_+ + N_-)/(N_+ - N_-)$ is the pair multiplicity, and $N_+ > N_-$ is assumed. In order to keep balance, $E_\parallel \sim N_- e/\Delta^2 \sim N_+ e/\Delta^2$ is required. The particle number in a coherent bunch is

$$N \sim \pi\mathcal{M}n_{\rm GJ}\Delta_\perp^2\Delta \sim 6\times10^{19}\mathcal{M}_4 B_{p,14}P_0^{-1}r_9^{-2}\nu_9^{-1}\Delta_1, \quad (7)$$

where $n_{\rm GJ} = (B_p/Pec)(r/R)^{-3}$ is the Goldreich–Julian density, $\Delta_\perp \sim \sqrt{r\lambda}$ is the maximum transverse size for a bunch-emitting coherent radiation. The parallel electric field is required to be

$$E_\parallel \sim \frac{Ne}{\Delta^2} \sim 5\times10^8\ \mathrm{V\ cm^{-1}} N_{20}\Delta_1^{-2}. \quad (8)$$

This value is greater than that estimated by Kumar et al. (2017) for the same parameters, since the existence of a screening electric field due to charge separation raises the demand of $E_\parallel$. With these parameters, the isotropic equivalent luminosity is given by

$$L_{\rm iso} \sim \eta N^2\gamma^4\frac{2e^2c\gamma^4}{3\rho^2} \sim 5\times10^{37}\ \mathrm{erg\ s^{-1}}\eta N_{20}^2\gamma_3^8\rho_9^{-2}, \quad (9)$$

where the factor of γ^4 is attributed to the radiation beaming effect (within a cone of half opening angle $1/\gamma$) and the relativistic propagation effect (by a factor of γ^2) (Kumar et al. 2017). This is consistent with the isotropic luminosity of FRB 200428.

In the model invoking Alfvén-wave-induced $E_\parallel$ (Lu et al. 2020), the FRB duration is determined by shear wave propagation inside the magnetar crust, i.e., $\tau \sim R/v \sim 3$ ms for the wave speed of $v \sim 0.01c$. The typical frequency of Alfvén waves may be $\nu_{\rm A} \sim (10^3$–$10^5)$ Hz, and the $E_\parallel$ in the charge starvation region would oscillate with a frequency of $\sim\nu_{\rm A}$ (Kumar & Bošnjak 2020). The pair-separation process delineated above would repeat itself within the millisecond duration of the FRB. One may estimate that there are approximately $\tau\nu_{\rm A} \sim$ (3–300) oscillations to contribute to the observed FRB emission.

Last, we check whether an FRB produced this way can propagate in the pair plasma inside the magnetosphere. We consider that the pair plasma is streaming relativistically with γ_s, and has an average spread of the background distribution in the plasma rest frame K', i.e., $\langle\gamma\rangle \sim \gamma/\gamma_s$. In the K' frame, the plasma frequency is

$$\omega_p' = \sqrt{\frac{4\pi e^2\mathcal{M}n_{\rm GJ}}{\gamma_s m_e}} \simeq 5\times10^7\ \mathrm{rad\ s^{-1}}\mathcal{M}_4^{1/2}B_{p,14}^{1/2}P_0^{-1/2}r_9^{-3/2}\gamma_{s,2}^{-1/2}. \quad (10)$$

According to the two-stream instability, in the laboratory frame the longitudinal size of a typical clump is

$$l \sim \frac{c}{\gamma_s\omega_p'} \simeq 6\ \mathrm{cm}\ \mathcal{M}_4^{-1/2}B_{p,14}^{-1/2}P_0^{1/2}r_9^{3/2}\gamma_{s,2}^{-1/2}, \quad (11)$$

which is also consistent with the above discussion about the pair separation. On the other hand, in the K' frame the Larmor frequency is

$$\omega_B' = \frac{eB_p}{m_e c}\left(\frac{r}{R}\right)^{-3} \simeq 1.8\times10^{12}\ \mathrm{rad\ s^{-1}}B_{p,14}r_9^{-3}, \quad (12)$$

and the FRB frequency is

$$\omega' = 2\pi\nu/\gamma_s \simeq 6\times10^7\ \mathrm{rad\ s^{-1}}\gamma_{s,-2}^{-1}. \quad (13)$$

Thus, $\omega_p' \sim \omega' \ll \omega_B'$ is satisfied. Since the polarized direction of curvature radiation is in the trajectory plane, the curvature radiation photons should be O-mode in the emission region. In a magnetized pair plasma, the transparency condition for O-mode photons is (Rafat et al. 2019)

$$\omega' > \frac{\omega_p'}{\sqrt{\langle\gamma\rangle}}\sin\theta_B \simeq 1.5\times10^6\ \mathrm{rad\ s^{-1}}\mathcal{M}_4^{1/2}B_{p,14}^{1/2} \times P_0^{-1/2}r_9^{-3/2}\gamma_3^{-1/2}\theta_{B,-1}, \quad (14)$$

where θ_B is the angle between the field line and photon momentum direction. Since $\theta \ll 1$ for the photons generated by curvature radiation, the pair plasma is transparent for the curvature radiation close to the emission region. As the photons propagate outward, the plasma frequency ω_p' would decrease (although θ increases slightly). The transparent condition is therefore always satisfied along the trajectory of wave propagation.

3. Coherent Radiation from the Separated Electron/Positron Bunches

Yang & Zhang (2018) calculated the coherent curvature radiation spectra of electron–positron pair bunches and derived a typical $S_\nu \propto \nu^{2/3}$ spectral shape in the low-energy regime. Such a spectral shape corresponds to a relatively wide spectrum, which may be in conflict with the nondetection of low-frequency FRBs so far (e.g., Tingay et al. 2015; Ravi et al. 2019). In the following, we improve the calculations by introducing the spatial separation of electron–positron pairs.

We calculate coherent radiation directly from the acceleration of charged particles. We assume that there are N charged particles moving along a trajectory $\boldsymbol{r}(t)$. The energy radiated per unit frequency interval per unit solid angle is given by (e.g., Jackson 1975)

$$\frac{dI}{d\omega d\Omega} = \frac{\omega^2}{4\pi^2 c}\left|\int_{-\infty}^{+\infty}\sum_j^N q_j\boldsymbol{n}\times(\boldsymbol{n}\times\boldsymbol{\beta}_j)e^{i\omega(t-\boldsymbol{n}\cdot\boldsymbol{r}_j(t)/c)}dt\right|^2, \quad (15)$$

where q_j is the corresponding charge, j represents the identifier of each charged particle, ω is the observed angle frequency, $\boldsymbol{n}$ is

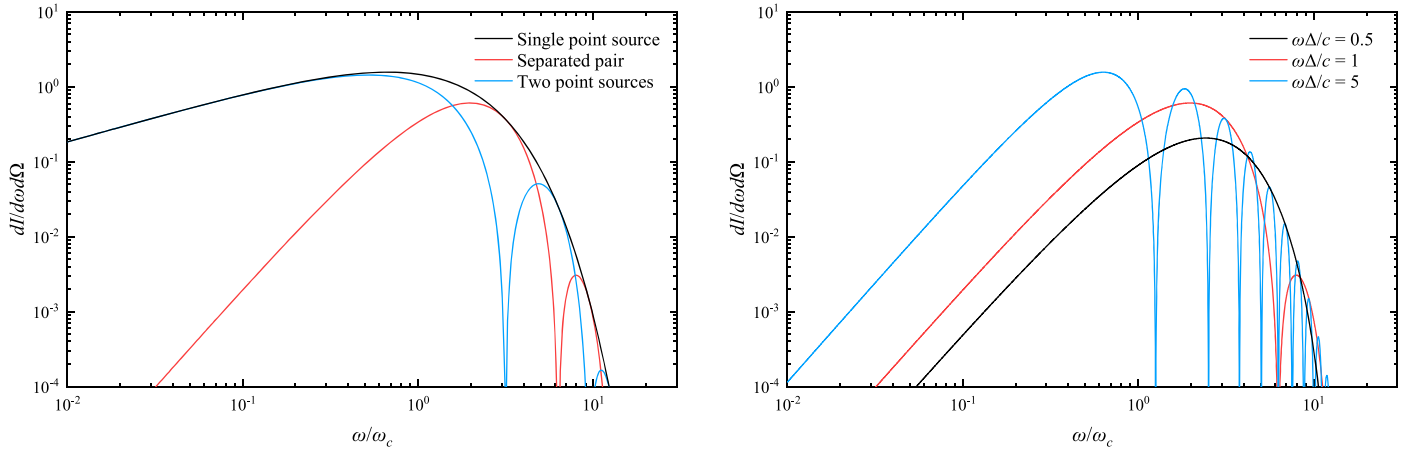

Figure 2. Left panel: coherent curvature radiation spectra for different bunches: a single point-source bunch (black line), from two charged-separated clumps with opposite signs (red line), and from two charge-separated clumps with the same sign (blue line). The unit of $dI/d\omega\, d\Omega$ is arbitrary. Right panel: coherent curvature radiation spectra for a pair of charge-separated clumps with different separation lengths. The black, red, and blue lines correspond to $\omega\Delta/c = 0.5$, 1, 5, respectively.

the unit vector between the electron and the observation point, and $\boldsymbol{\beta} = \dot{\boldsymbol{r}}(t)/c$ is the dimensionless velocity.

We consider the coherent emission from a pair of charge-separated clumps, as shown in Figure 1. For simplicity, we assume both the electron clump and positron clump as point sources with a separation Δ. We take the electron/positron number in each clump as N, then the coherent radiation from the pair of clumps can be calculated by

$$\frac{dI_{(N)}}{d\omega d\Omega} = \frac{N^2 e^2 \omega^2}{4\pi^2 c}\left|\int_{-\infty}^{+\infty} \boldsymbol{n}\times(\boldsymbol{n}\times\boldsymbol{\beta}) e^{i\omega(t-\boldsymbol{n}\cdot\boldsymbol{r}(t)/c)}dt\right|^2 \times |1 - e^{-i\omega(\boldsymbol{n}\cdot\boldsymbol{\Delta}/c)}|^2. \quad (16)$$

This equation can be written as the radiation of a single electron multiplied by a coherent factor $|1 - e^{-i\omega(\boldsymbol{n}\cdot\boldsymbol{\Delta}/c)}|^2 N^2 = 2[1 - \cos(\omega\boldsymbol{n}\cdot\boldsymbol{\Delta}/c)]N^2$, i.e.,

$$\frac{dI_{(N)}}{d\omega d\Omega} = 2\left[1 - \cos\left(\frac{\omega\boldsymbol{n}\cdot\boldsymbol{\Delta}}{c}\right)\right]N^2\frac{dI_{(1)}}{d\omega d\Omega}, \quad (17)$$

where the radiation from a single electron satisfies $dI_{(1)}/d\omega d\Omega \propto \omega^{2/3}\exp(-\omega/\omega_c)$ (e.g., Yang & Zhang 2018), and $\omega_c = 3\gamma^3 c/2\rho$ is the critical frequency. We consider that the observed energy reaches the maximum value when the line of sight is parallel to the trajectory plane, i.e., $\boldsymbol{n}\cdot\boldsymbol{\Delta} = \Delta$. For $\omega\Delta/c \ll 1$, one has

$$\frac{dI_{(N)}}{d\omega d\Omega} \propto \omega^{8/3} \quad \text{for } \omega \ll \omega_l \ll \omega_c, \quad (18)$$

where

$$\omega_l \sim c/\Delta. \quad (19)$$

We can see that the low-frequency spectrum is much harder than $S_\nu \propto \nu^{2/3}$, which appears as a narrow spectrum compared with the classical curvature radiation.

On the other hand, in order to make the radiation from the charge-separated clump pair coherent, the condition $\Delta/\rho \ll \theta_c$ needs to be satisfied, where $\theta_c \sim (3c/\omega\rho)^{1/3}$ is the emission angle in the $\omega \ll \omega_c$ regime. Therefore, the upper limit of the coherent frequency is given by

$$\omega_m \sim \left(\frac{\rho}{\Delta}\right)^2 \omega_l. \quad (20)$$

Electromagnetic waves with $\omega \gg \omega_m$ would not be coherent between the two clumps, even though they could be coherent within each clump individually. It is worth checking whether two adjacent clump pairs are coherent. For the Alfvén wave with a frequency of $\nu_A \sim (10^3$–$10^5)$ Hz, the separation between the two pairs is $L \sim c/\nu_A$, giving the maximum coherent frequency

$$\nu_M \sim \frac{c\rho^2}{2\pi L^3} \sim \frac{\rho^2\nu_A^3}{2\pi c^2} \simeq 0.2\ \text{GHz}\ \rho_9^2\nu_{A,4}^3. \quad (21)$$

Therefore, the radiation from two adjacent clump pairs is essentially incoherent.

In the left panel of Figure 2, we plot the coherent curvature radiation spectra for several different bunches: a single point-source bunch (black line), from two charged-separated clumps with opposite signs (red line), and from two charge-separated clumps with the same sign (blue line). First, we compare the case of one bunch and two bunches with the same sign of charge. Due to the spatial distribution of the charged sources, some narrow spectral structures appear (Katz 2018; Yang & Zhang 2018). However, in general the complete spectrum for two bunches is still wide, with $S_\nu \propto \nu^{2/3}$ at low frequencies. On the other hand, if the two bunches have opposite charges, as expected for charge separation in an external $E_\parallel$, the low-frequency radiation is suppressed and the final spectrum becomes narrow. In the right panel of Figure 2, we plot the coherent curvature radiation spectra of a pair of clumps with opposite charges for different separations. We can see that the spectral structure becomes progressively more complicated as the separation increases. On the other hand, the peak intensity also increases with Δ. This is because as the two clumps are close, the opposite charges tend to cancel out each other to suppress coherence. In any case, the low-frequency spectral index remains 8/3, maintaining a narrow spectrum.

For FRB 200428 from SGR J1935+2154, the CHIME burst shows an average fluence of 0.48 MJy ms for the first burst component and 0.22 MJy ms for the second burst component in the frequency band (400–800) MHz (The CHIME/FRB

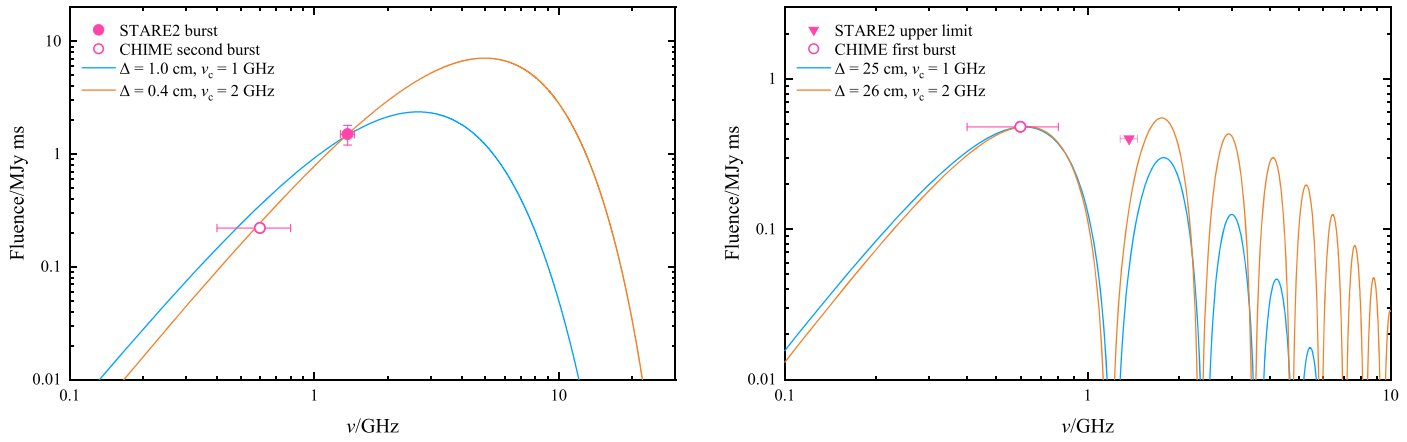

Figure 3. Application of this model to FRB 200428. Left panel: the spectrum derived from the CHIME second burst and the STARE2 burst. The blue line corresponds to $\Delta = 1.0$ cm and $\nu_c = 1$ GHz. The orange line corresponds to $\Delta = 0.4$ cm and $\nu_c = 2$ GHz. Right panel: the spectrum derived from the CHIME first burst and the STARE2 upper limit. The blue line corresponds to $\Delta = 25$ cm and $\nu_c = 1$ GHz. The orange line corresponds to $\Delta = 26$ cm and $\nu_c = 2$ GHz.

Collaboration et al. 2020). The STARE2 burst shows an average fluence of 1.5 ± 0.3 MJy ms at a frequency band of (1281–1468) MHz. Assuming that the STARE2 burst corresponds to the second CHIME burst component, the upper limit on the first CHIME burst component is 0.4 MJy ms in the STARE2 frequency band (Bochenek et al. 2020).

The spectral feature of FRB 200428 can be interpreted within the framework of our model. As shown in the left panel of Figure 3, the observational spectrum constructed from the CHIME and STARE2 data for the second burst component is consistent with the low-frequency spectrum predicted by Equation (17), with a spectral index of 8/3. For the critical frequencies of $\nu_c = 1$ GHz and $\nu_c = 2$ GHz, the pair separation is required to be $\Delta = 1.0$ cm and $\Delta = 0.4$ cm, respectively. For given observational data, the larger the critical frequency, the smaller the required separation between the clump pair. On the other hand, for the first burst component, the observed fluence decreases as frequency increases (see Figure 1 in The CHIME/FRB Collaboration et al. 2020). Meanwhile, STARE2 did not detect this component and only gives an upper limit. The constructed spectrum for this component can be accommodated by our model assuming that the CHIME band is around the first peak frequency. As shown in the right panel of Figure 3, the data are consistent with the model for different values of the critical frequency. For $\nu_c = 1$ GHz and $\nu_c = 2$ GHz, the clump separation is required to be $\Delta = 25$ cm and $\Delta = 26$ cm, respectively. The smaller the critical frequency, the lower the fluence of high-frequency oscillations.

4. Summary

Prompted by the association of the two bursts of FRB 200428 with the two X-ray peaks in the lightcurve of its X-ray counterpart (Li et al. 2020), we further develop the magnetospheric model of FRBs (Kumar et al. 2017; Yang & Zhang 2018) by introducing charge separation of pairs in a parallel electric field due to charge starvation of an Alfvén wave (Kumar & Bošnjak 2020; Lu et al. 2020). By calculating coherent emission from first principles, we obtain a narrow spectrum with low-frequency spectral index 8/3. This model is found to be able to interpret the observed spectra of the two components of FRB 200428 (Bochenek et al. 2020; The CHIME/FRB Collaboration et al. 2020). The model may also give interpretations to other FRBs that have evidence of narrow spectra (e.g., Spitler et al. 2016).

We thank Pawan Kumar, Wenbin Lu, and a referee for valuable comments and discussions. This work is partially supported by the National Natural Science Foundation of China under grant No. 11725314 and the National Basic Research Program of China under grant No. 2014CB845800.

ORCID iDs

Yuan-Pei Yang https://orcid.org/0000-0001-6374-8313
Jin-Ping Zhu https://orcid.org/0000-0002-9195-4904
Bing Zhang https://orcid.org/0000-0002-9725-2524
Xue-Feng Wu https://orcid.org/0000-0002-6299-1263

References

Arons, J., & Scharlemann, E. T. 1979, ApJ, 231, 854
Bannister, K. W., Deller, A. T., Phillips, C., et al. 2019, Sci, 365, 565
Beloborodov, A. M. 2009, ApJ, 703, 1044
Beloborodov, A. M. 2017, ApJL, 843, L26
Beloborodov, A. M. 2020, ApJ, 896, 142
Beloborodov, A. M., & Thompson, C. 2007, ApJ, 657, 967
Bochenek, C. D., Ravi, V., Belov, K. V., et al. 2020, arXiv:2005.10828
Camilo, F., Ransom, S. M., Halpern, J. P., et al. 2006, Natur, 442, 892
Camilo, F., Ransom, S. M., Halpern, J. P., & Reynolds, J. 2007, ApJL, 666, L93
Chatterjee, S., Law, C. J., Wharton, R. S., et al. 2017, Natur, 541, 58
Cordes, J. M., & Wasserman, I. 2016, MNRAS, 457, 232
Dai, Z. G. 2020, ApJL, 897, L40
Hessels, J. W. T., Spitler, L. G., Seymour, A. D., et al. 2019, ApJL, 876, L23
Jackson, J. D. 1975, Classical Electrodynamics (New York: Wiley)
Katz, J. I. 2016, ApJ, 826, 226
Katz, J. I. 2018, MNRAS, 481, 2946
Kumar, P., & Bošnjak, Ž 2020, MNRAS, 494, 2385
Kumar, P., Lu, W., & Bhattacharya, M. 2017, MNRAS, 468, 2726
Li, C. K., Lin, L., Xiong, S. L., et al. 2020, arXiv:2005.11071
Lin, L., Zhang, C. F., Wang, P., et al. 2020, arXiv:2005.11479
Lorimer, D. R., Bailes, M., McLaughlin, M. A., Narkevic, D. J., & Crawford, F. 2007, Sci, 318, 777
Lu, W., & Kumar, P. 2018, MNRAS, 477, 2470
Lu, W., Kumar, P., & Zhang, B. 2020, arXiv:2005.06736
Lyubarsky, Y. 2014, MNRAS, 442, L9
Marcote, B., Nimmo, K., Hessels, J. W. T., et al. 2020, Natur, 577, 190
Margalit, B., Beniamini, P., Sridhar, N., & Metzger, B. D. 2020, ApJL, 899, L27
Mereghetti, S., Savchenko, V., Ferrigno, C., et al. 2020, ApJL, 898, L29
Metzger, B. D., Margalit, B., & Sironi, L. 2019, MNRAS, 485, 4091
Pen, U.-L., & Connor, L. 2015, ApJ, 807, 179

Prochaska, J. X., Macquart, J.-P., McQuinn, M., et al. 2019, Sci, 366, 231
Rafat, M. Z., Melrose, D. B., & Mastrano, A. 2019, JPlPh, 85, 905850305
Ravi, V., Catha, M., D'Addario, L., et al. 2019, Natur, 572, 352
Ridnaia, A., Svinkin, D., Frederiks, D., et al. 2020, arXiv:2005.11178
Ruderman, M. A., & Sutherland, P. G. 1975, ApJ, 196, 51
Spitler, L. G., Scholz, P., Hessels, J. W. T., et al. 2016, Natur, 531, 202
Tavani, M., Casentini, C., Ursi, A., et al. 2020, arXiv:2005.12164
The CHIME/FRB Collaboration, Andersen, B. C., Bandura, K. M., et al. 2020, arXiv:2005.10324
Thompson, C., & Beloborodov, A. M. 2005, ApJ, 634, 565
Thompson, C., Lyutikov, M., & Kulkarni, S. R. 2002, ApJ, 574, 332
Thornton, D., Stappers, B., Bailes, M., et al. 2013, Sci, 341, 53
Tingay, S. J., Trott, C. M., Wayth, R. B., et al. 2015, AJ, 150, 199
Wadiasingh, Z., Beniamini, P., Timokhin, A., et al. 2020, ApJ, 891, 82
Wang, J.-S. 2020, arXiv:2006.14503
Wang, W., Zhang, B., Chen, X., & Xu, R. 2019a, ApJ, 875, 84
Wang, W., Zhang, B., Chen, X., & Xu, R. 2019b, ApJL, 876, L15
Wang, W.-Y., Xu, R., Zheng, X., & Chen, X. 2020, ApJ, 899, 109
Waxman, E. 2017, ApJ, 842, 34
Wu, Q., Zhang, G. Q., Wang, F. Y., & Dai, Z. G. 2020, ApJL, 900, L26
Yang, Y.-P., & Zhang, B. 2018, ApJ, 868, 31
Yu, Y.-W., Zou, Y.-C., Dai, Z.-G., & Yu, W.-F. 2020, arXiv:2006.00484
Zhang, B. 2017, ApJL, 836, L32